Supporting Information

Boosted charge transfer in Pt clusters anchored TiO$_2$ microspheres with rich oxygen vacancies for solar driven H$_2$ production from lignocellulosic biomass

Fu-Guang Zhang$^{a,\perp}$, Miao Cheng$^{b,\perp}$, Yong-Jun Yuan^{a,*} Qing-Yu Liu^a, Quan Cheng^a,

Jie Guan^{c,*}

^{a}College of Materials and Environmental Engineering, Hangzhou Dianzi University,

Hangzhou 310018, People's Republic of China.

^{b}School of Chemistry and Chemical Engineering, Southeast University, Nanjing

211189, People's Republic of China.

^{c}School of Physics, Southeast University, Nanjing 211189, People's Republic of China.

$^{\perp}$These authors contributed equally to this work.

*E-mail: yjyuan@hdu.edu.cn; guanjie@seu.edu.cn.

Experimental

Synthesis of porous TiO$_2$ microspheres.

Porous TiO$_2$ microspheres were prepared through a solvothermal method. In a typical preparation, titanium solution was prepared by dispersing of 3 ml of titanium isopropoxide in 30 ml of anhydrous acetone to obtain an orange transparent solution. After stirring for 10 minutes, the mixture solution was transferred into a 50 ml Teflon-lined stainless-steel autoclave which was heated at 200 °C for 4 h in an oven. After cooling to room temperature, the produced precipitate was collected by centrifugation at 4000 rpm and fully washed with deionized water and anhydrous acetone to remove impurity. The product was dried at 60° in vacuum drying oven. The white product was finally heated at 400 °C for 4 h under air atmosphere to remove the surface organic compounds.

Synthesis of Pt/TiO$_2$ photocatalyst.

In a typical synthesis of Pt/TiO$_2$ photocatalyst, 500 mg of as-synthesized TiO$_2$ microspheres was added in 100 mL deionized water and ultrasonically dispersed for 60 minutes to obtain a uniformly dispersed suspension solution. And then 2.5 mL of 2 mg·mL^{-1} K$_2$PtCl$_6$ solution was added into the above suspension solution, which was kept dark environment at 0 °C in an ice-bath with magnetic stirring for 4 h. The product was collected by centrifugation at 5000 rpm, then washed with deionized water and absolute ethanol, and finally dried at room temperature in vacuum drying oven to obtain faint yellow 1.0% Pt/TiO$_2$ photocatalyst. In addition, the 0.2%, 0.4%, 0.6%, 0.8% Pt/TiO$_2$ photocatalyst, respectively, were also synthesized through the same process except using 0.5, 1.0, 1.5 and 2.0 mL of 2 mg·mL^{-1} K$_2$PtCl$_6$ solution instead of 2.5 mL K$_2$PtCl$_6$ aqueous solution.

Photocatalytic lignocellulosic biomass-to-H$_2$ conversion experiments.

The photocatalytic lignocellulosic biomass-to-H$_2$ conversion experiments were performed under UV-Vis light irradiation (300 W Xe lamp, Shenyang Yilida Technology Co., LTD) in a 350 ml Pyrex photoreactor with a top window which connected to a closed gas-circulating vacuum system. Typically, 100 mg Pt/TiO$_2$

photocatalyst and 1g substance are added in a 250 ml of aqueous solution and ultrasonically dispersed for 30 minutes in the photoreactor. The lignocellulosic biomass including rice straw, wheat straw, polar wood chip, bamboo, rice hull and corncob were sieved on 80 mesh sifter, and the lignocellulosic biomass with size less than180 μm were used as substance for photocatalytic reaction. Prior to irradiation, the suspension solution was degassed to remove residual air. The temperature of photocatalytic H_2 production system was maintained at room temperature in the presence of a flow of cooling water. The evolved H_2 was analyzed by an on-line GC1690 gas chromatography with a TCD detector (Jiedao, 5 Å molecular sieves column, Ar as the carrier gas). For outdoor photocatalytic H_2 production experiments, the reaction solution was transferred into a sealed glass reactor, and the outdoor sunlight was used as light source. The evolved gas (1.0 ml) extracted from the headspace of reactor was injected into the GC to analyze the amount of H_2. The photocatalytic H_2 production experiment for the measurement of apparent quantum efficiency (AQY) was conducted by the same process expect using monochromatic light filter, and the AQY was calculated according to the following equations:

$$n_{\text{photons}} = \frac{P\lambda}{hc} \times t \tag{1}$$

$$AQY[\%] = \frac{\text{number of reacted electrons}}{\text{number of incident photons}} \times 100$$

$$= \frac{2 \times \text{number of evolved } H_2 \text{ molecules}}{\text{number of incident photons}} \times 100 \tag{2}$$

where *P, λ, h, c and t* is the input optical power, wavelength of the light, Planck's constant, speed of light and the illumination time, respectively.

Characterization. The crystalline structure of photocatalyst was examined with a Rigaku-miniflex 6 X-ray diffractometer (Japan) equipped with Cu *K*α (λ = 0.15406 nm) radiation. The Raman spectra were recorded on a J-Y T64000 Raman spectrometer equipped with 532 nm wavelength incident laser light. The morphology of materials was characterized on a field emission Hitachi S-4800 scanning electron microscope and JEOL JEM 2010 transmission electron microscope. Apherical aberration-corrected HAADF-STEM and EDX elemental mapping images of Pt/TiO$_2$ were performed by a JEOL JEM-ARM200F ARM electron microscope. The specific

surface area of sample was obtained from nitrogen adsorption-desorption isotherms measured at 77 K using a Micromeritics ASAP 2460 apparatus, the BET surface area was calculated from the adsorption data, and the pore distribution was calculated by the Barret-Joyner-Halenda method. The optical properties of photocatalysts were assessed by using Varian cary 500 UV-vis spectrophotometer by using $BaSO_4$ as the background. The XPS measurements were analyzed on a Thermo ESCALAB 250XI XPS system with Al Kα X-ray source. Transient photocurrent measurements were carried out a standard three-electrode system with a saturated Ag/AgCl electrode as the reference electrode, Pt wire as the counter electrode and sample-coated ITO glass as working electrode using a CHI660E electrochemical workstation (Shanghai Chenhua Limited, China) with an external voltage of 0.5 V vs. RHE. A 0.5 M Na_2SO_4 aqueous solution was used as electrolyte, and all measured potentials (vs. AgCl/Ag) were converted to the potentials versus the RHE. The working electrode was prepared by coating the suspension solution of photocatalyst (1 mg·ml^{-1}) on the ITO glass, and dried at room temperature. The LSV plots were performed in 0.5 M H_2SO_4 aqueous solution in standard three-electrode system as described above expect the use of sample coated platinized carbon electrode as the working electrode. For the CO_2 detection, 1 ml gas extracted from the reaction system was detected by a carbon dioxide analyzer (AR8200, Smart Seneor, China). The high performance liquid chromatography (HPLC) analysis was performed on an Agilent HPLC 1260 chromatographic instrument. The total organic carbon (TOC) analysis of solution was carried on a Vario TOC analyzer (Elementar, Germany).

Theoretical methods

All our first principles calculations were carried out within the framework of density functional theory (DFT) as implemented in "Vienna ab initio simulation package" (VASP).[1,2] Perdew-Burke-Ernzerhof (PBE) exchange-correlation functional were used and the van der Waals (vdW) force was also considered with the usage of DFT-D3 method.[3,4] Projector-augmented-wave (PAW) pseudopotentialsand a plane-wave basis set with cutoff energy of 500 eV were used.[5,6]   A vacuum spacing of 20 Å was employed to eliminate the interactions between layers. A total

energy difference between subsequent self-consistency iterations below 10^{-5} eV is used as the criterion for reaching self-consistency. All geometries have been optimized using the conjugate-gradient (CG) method,[7] until none of the residual Hellmann-Feynman forces exceeded 10^{-2} eV/Å. The Gaussian smearing width was set to 0.1 eV. A 4 × 4 supercell slab consisting of 96 atoms was used in this study to represent the anatase TiO_2 (101) surface. The Brillouin zone was sampled with a 3×3×1 Monkhorst-Pack grid.[8]

Gibbs free energy change (ΔG) of each chemical reaction step was calculated by:

$$\Delta G = \Delta E\_DFT + \Delta E\_ZPE - T\Delta S,$$

where ΔE_DFT, ΔE_ZPE, T, and S denote the calculated total energy, zero-point energy, temperature, and entropy, respectively. Adsorption energy ΔE_DFT on the surface of substrates was defined as:

$$\Delta E\_DFT = E\_(*H_2O) - (E\_* + E\_(H_2O)),$$

where $E\_(*H_2O)$, E_*, and $E\_(H_2O)$ denote the total energies of H_2O molecule attached on substrates, bare substrates, and isolated H_2O molecule. The zero-point energy and entropy were calculated using VASPKIT code.[9]
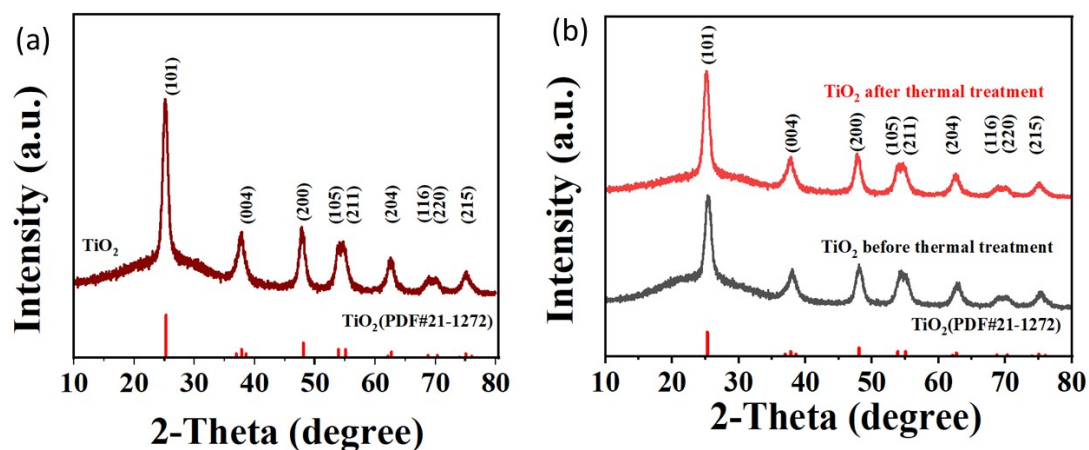
Figure S1. (a) XRD pattern of bare TiO$_2$ prepared from solvothermal reaction. (b) XRD pattern of bare TiO$_2$ before and after thermal treatment at 400 ^oC for 4h under air atmosphere

Figure S2. XRD pattern of bare TiO$_2$ and Pt/TiO$_2$ photocatalysts loaded with various Pt nanoclusters.
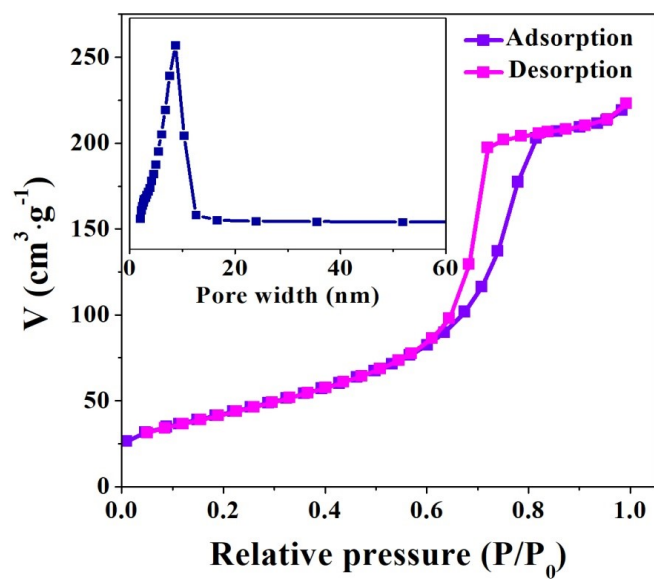
Figure S3. N_2 adsorption-desorption curve of as-prepared porous TiO_2 microspheres, the inset is the BJH pore size distribution.
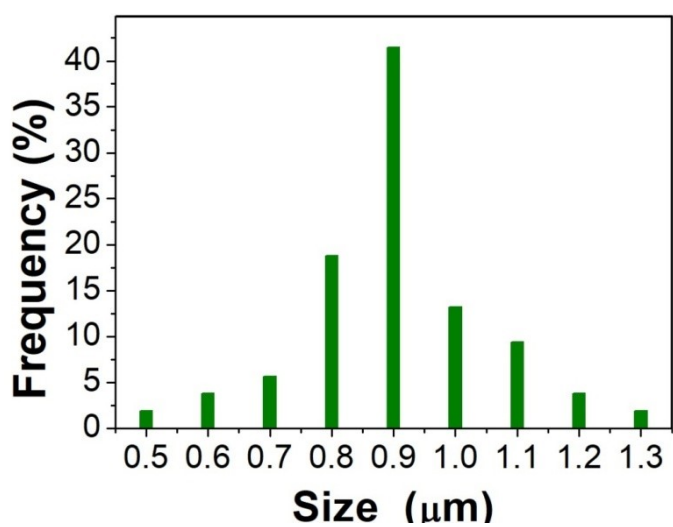
Figure S4. The size distribution of bare TiO_2 microspheres obtained from Figure 1b.
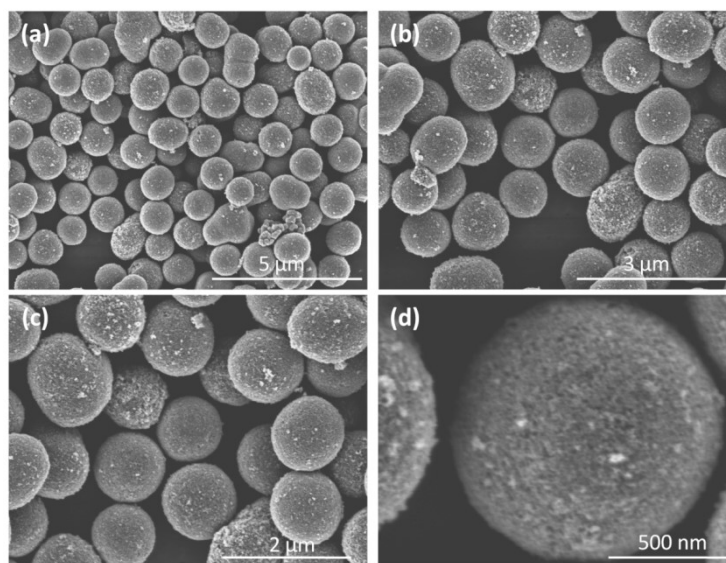
Figure S5. SEM images of bare TiO_2 obtained from solvothermal reaction.
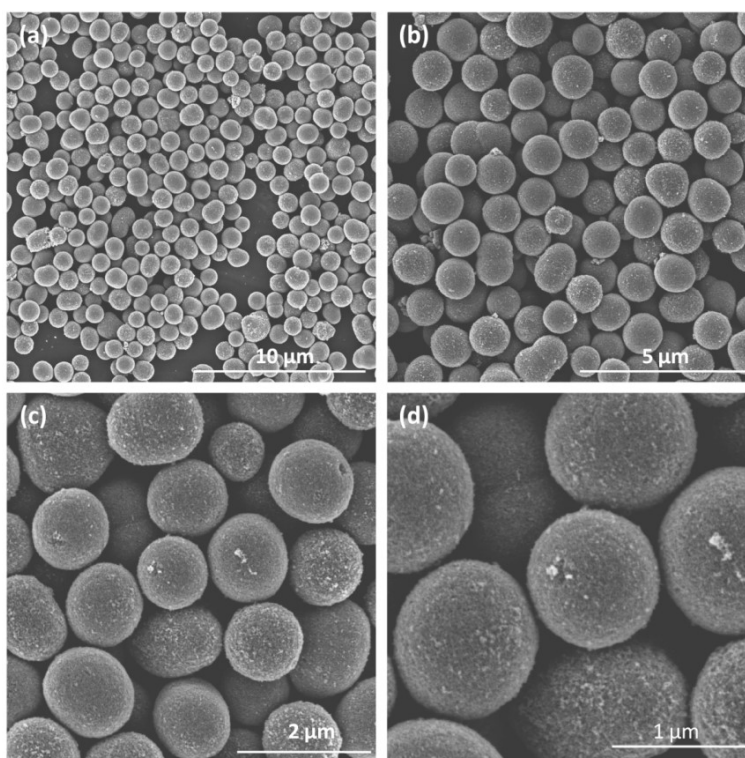
Figure S6. SEM images of bare TiO_2 after thermal treatment at 400 °C for 4h under air atmosphere.
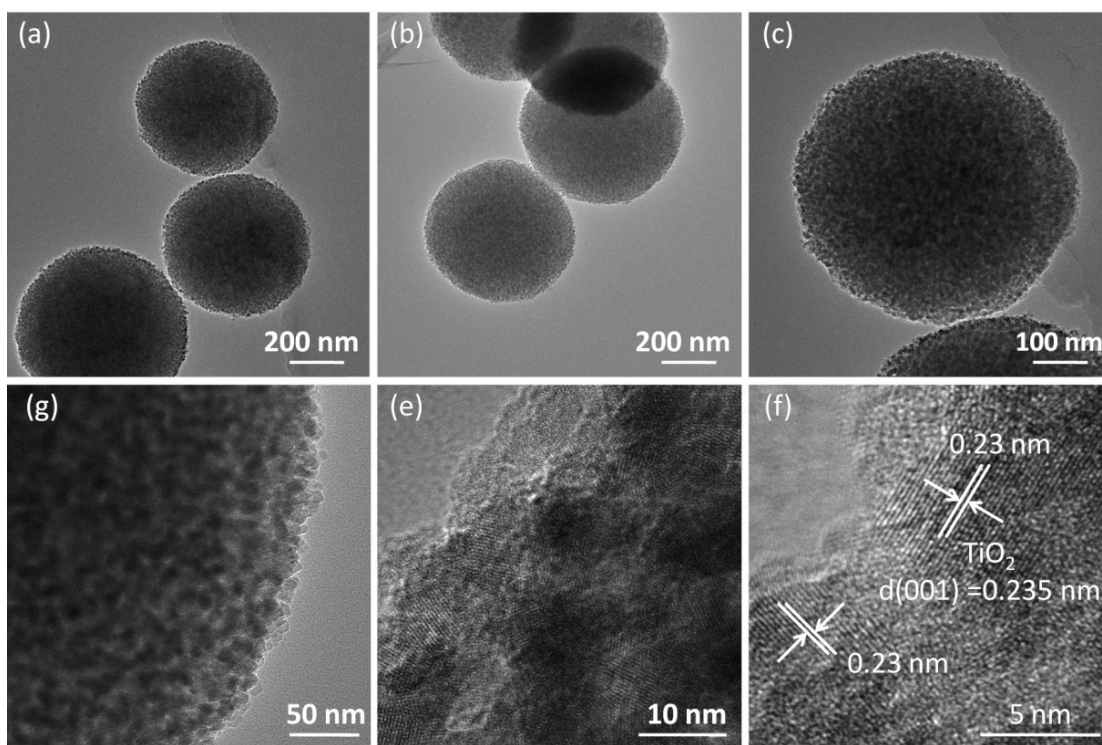
Figure S7. (a-e) TEM and (f) high resolution TEM images of bare TiO_2 microsphere.
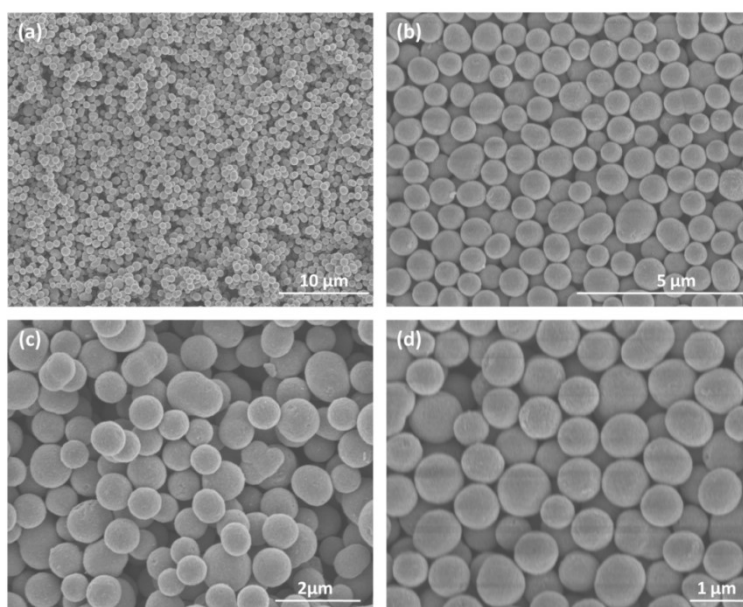
Figure S8. (a-d) SEM images of 0.4% Pt/TiO_2 photocatalyst.
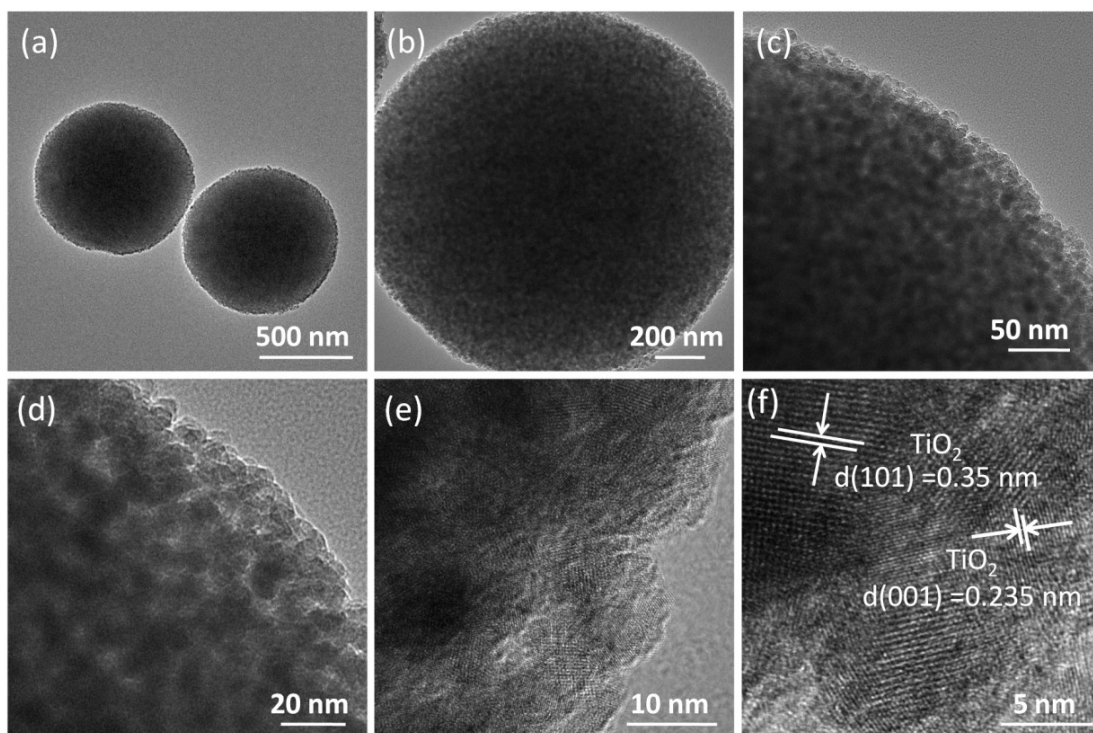
Figure S9. (a-e) TEM and high resolution TEM images (f) of 0.4% Pt/TiO$_2$ photocatalyst.
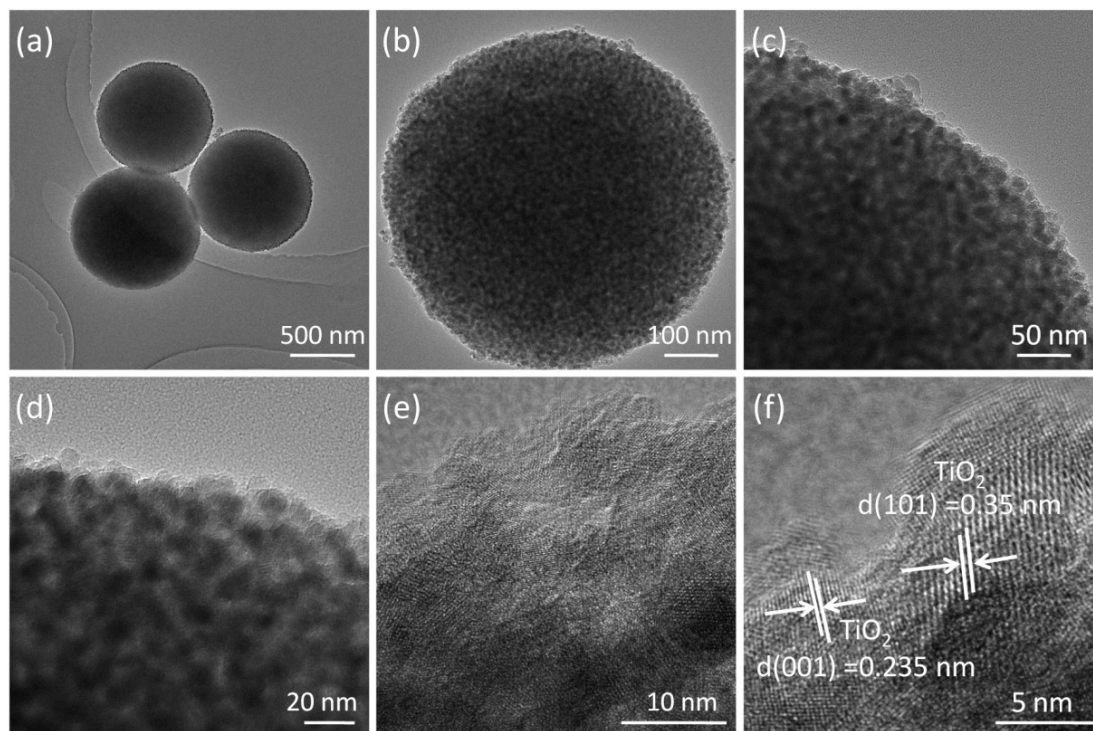
Figure S10. (a-e) TEM and (f) high resolution TEM image of 0.6% Pt/TiO$_2$ photocatalyst.
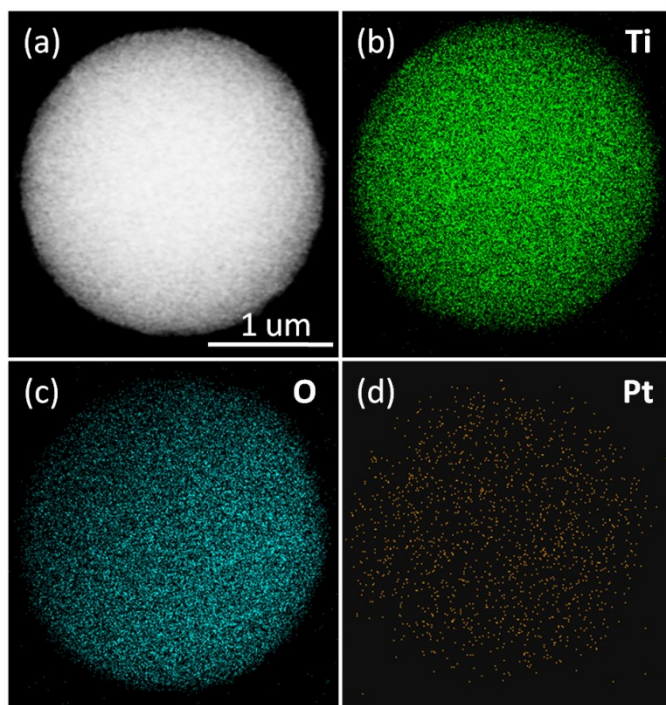
Figure S11. (a-d) HADDF image of 0.4% Pt/TiO$_2$ and corresponding elemental mapping for Ti (b), O (c) and P (d).
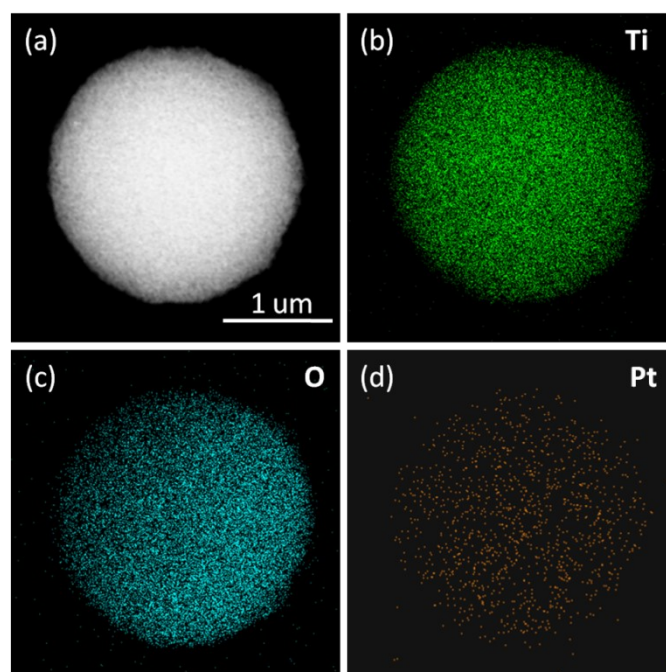
Figure S12. (a-d) HADDF image of 0.6% Pt/TiO$_2$ and corresponding elemental mapping for Ti (b), O (c) and P (d).
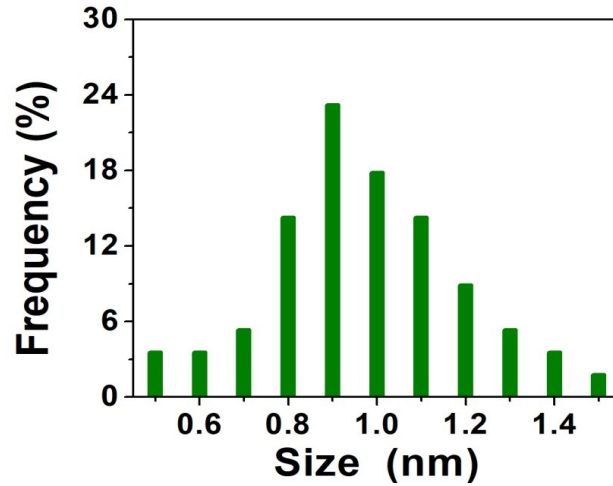
Figure S13. The size distribution of Pt in 0.4% Pt/TiO$_2$ photocatalyst obtained from Figure 2e.
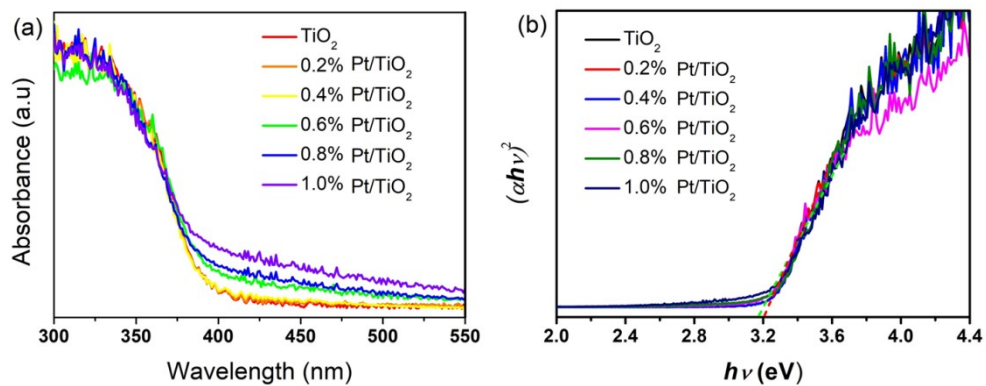
Figure S14. (a) UV-Vis spectra of Pt/TiO$_2$ photocatalysts loaded with various amount of Pt; (b) Bandgap of Pt/TiO$_2$ photocatalysts estimated by a related curve of $(\alpha h\nu)^2$ versus photon energy. Although the Pt/TiO$_2$ samples exhibit poor visible light absorption, the bandgap Pt/TiO$_2$ photocatalysts does not show obvious red-shift as compared to that of bare TiO$_2$. The bandgap of bare TiO$_2$ and the 0.4% Pt was estimated to be 3.20 (red line) and 3.17 eV (green line), respectively.
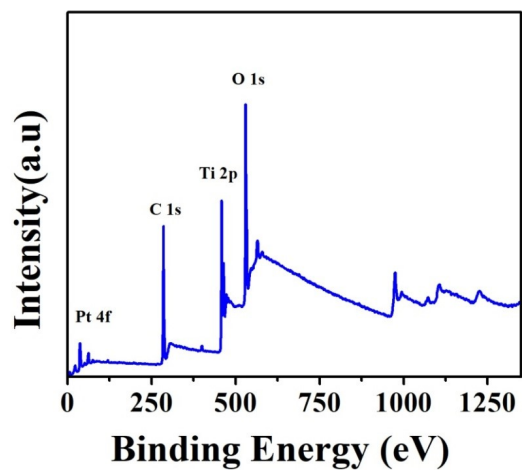
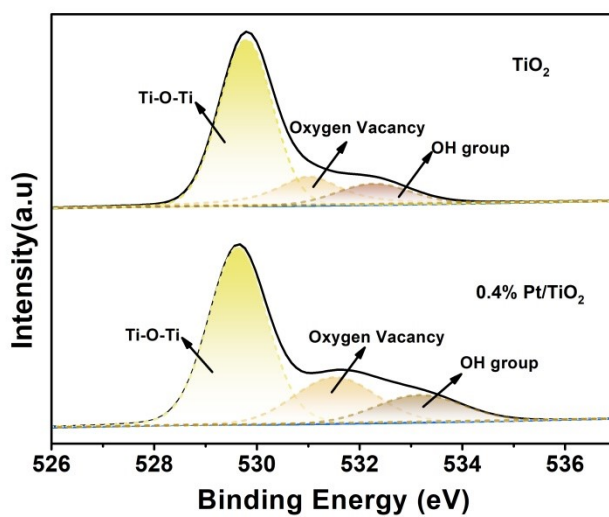**Figure S15**. The survey XPS spectrum for 0.4% Pt/TiO$_2$ photocatalyst.

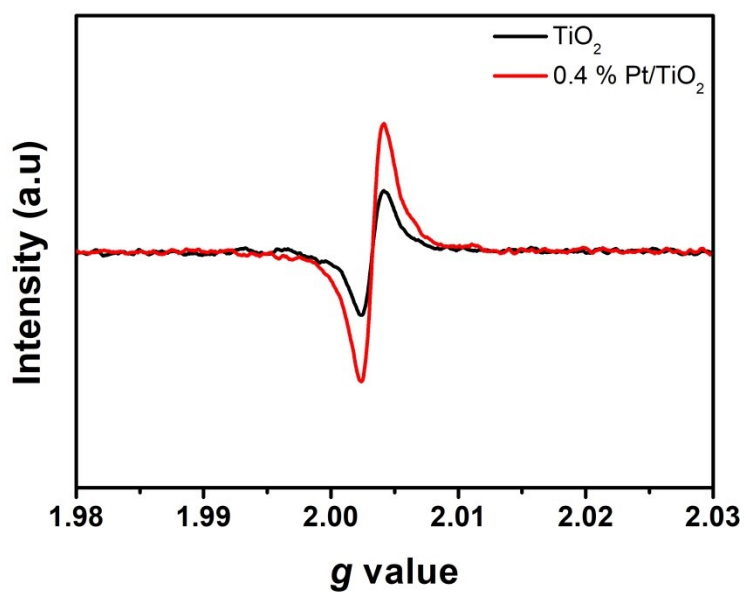**Figure S16.** Comparison of high-resolution O 1s XPS spectra of 0.4% Pt/TiO$_2$ with bare TiO$_2$.

Figure S17. EPR spectra of TiO_2 and 0.4% Pt/TiO_2.
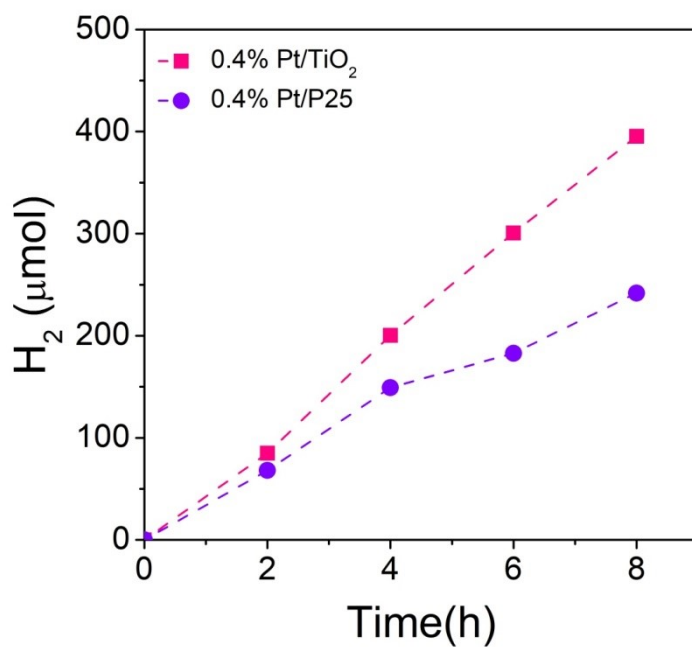

Figure S18. Comparison of photocatalytic H_2 generation activity of 0.4 Pt/TiO_2 photocatalyst with 0.4% Pt/P25 sample. Photocatalytic reaction conditions: 100 mg photocatalyst, 300 W Xe lamp, 1g α-cellulose, 250 ml water.

Figure S19.   Photograph of photocatalytic experiment conducted by using sunlight as light source.
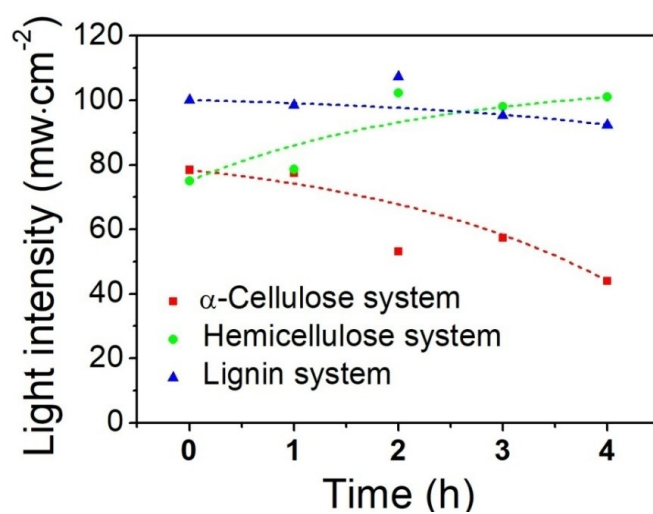

Figure S20. Light intensity of sunlight outdoors for photocatalytic H_2 production in a α-cellulose, hemicellulose, lignin system corresponding to Figure 4c.
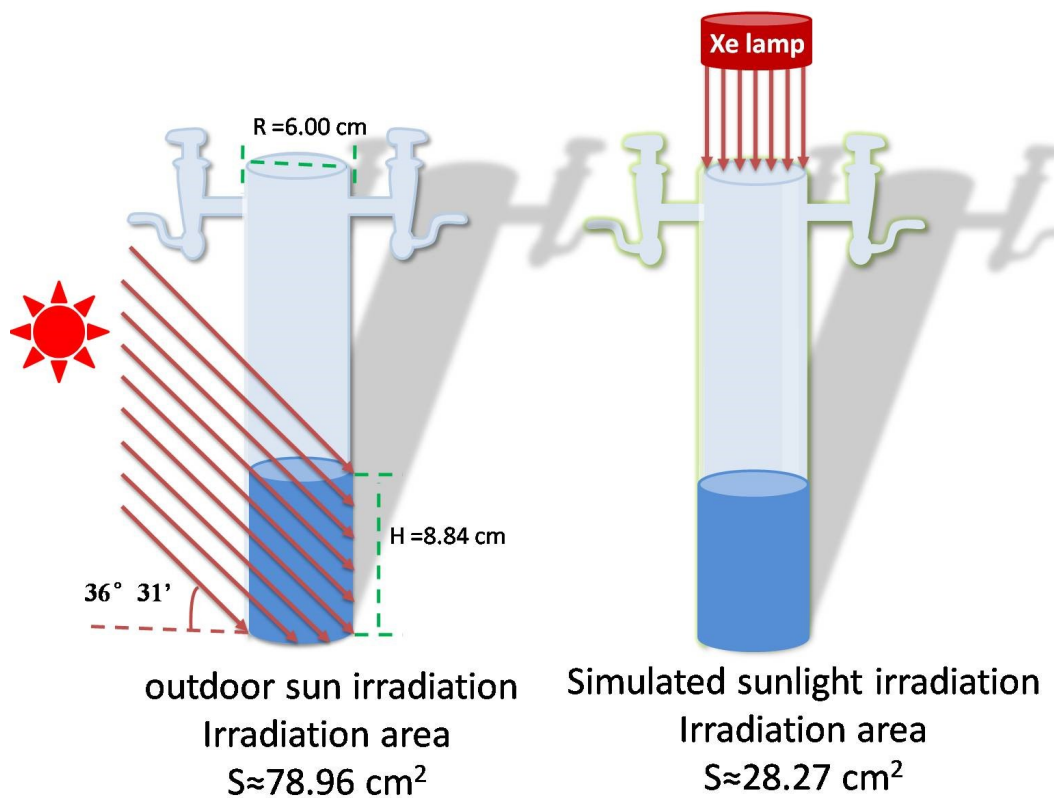
Figure S21. Schematic diagram of irradiation area under simulated sunlight irradiation and outdoor sun irradiation. For simulated sunlight irradiation, the light power was 2827 mW (28.27 cm^2 × 100 mw·cm^2), for outdoor sun irradiation, the light power ranged from 4959 (78.96 cm^2 × 62.8 mw·cm^2) to 7795 mW (78.96 cm^2 × 98.72 mw·cm^2) when the averaged light intensity was ranged from 62.8 to 98.72 mw·cm^2 estimate from Figure S22.
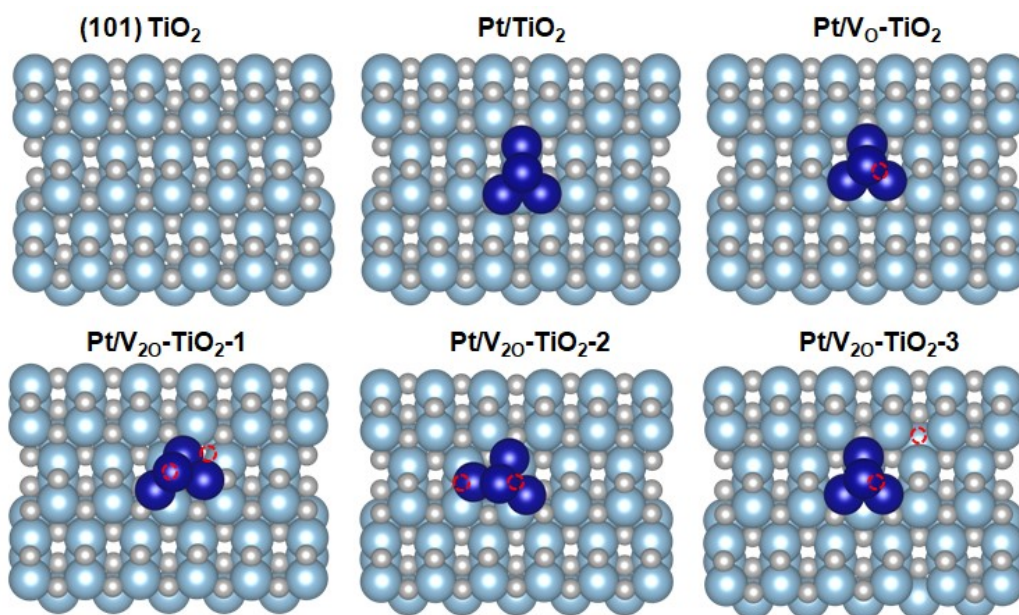
Figure S22. Structural models of TiO$_2$ (101) surface, Pt/TiO$_2$, Pt/V$_O$-TiO$_2$, Pt/V$_{2O}$-TiO$_2$-1, Pt/V$_{2O}$-TiO$_2$-2, and Pt/V$_{2O}$-TiO$_2$-3. The location of the O-vacancies is marked by dashed red circles.
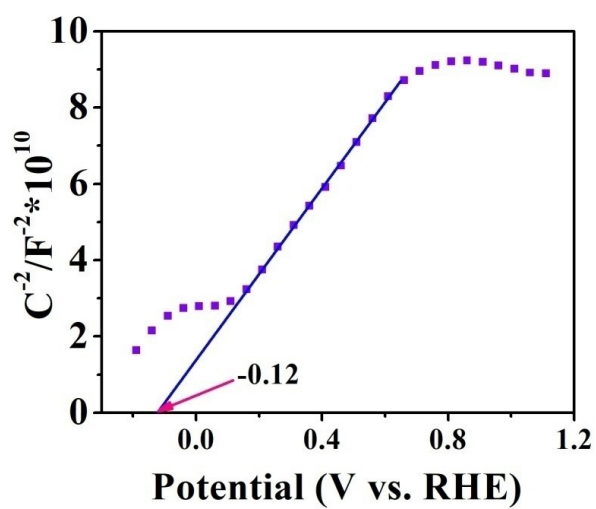

Figure S23. Mott-Schottky plots of TiO$_2$ electrode measured in Na$_2$SO$_4$ aqueous solution.
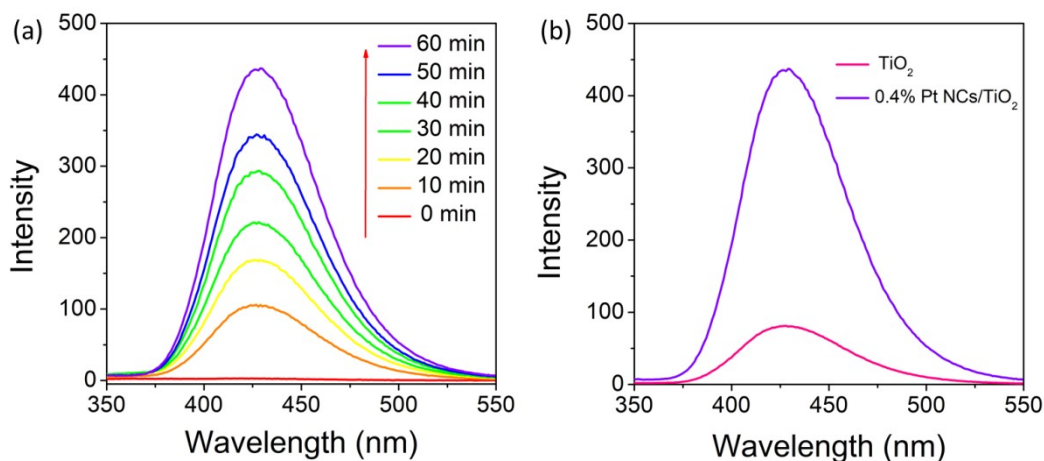
Figure S24. (a) PL spectrum of TAOH collected from the photocatalytic system in the presence of 0.4% Pt NCs/TiO$_2$ after different irradiation time. (b) Comparison of PL spectrum of TAOH collected from the photocatalytic system in the presence of bare TiO$_2$ and 0.4% Pt NCs/TiO$_2$ after 1 h of irradiation.
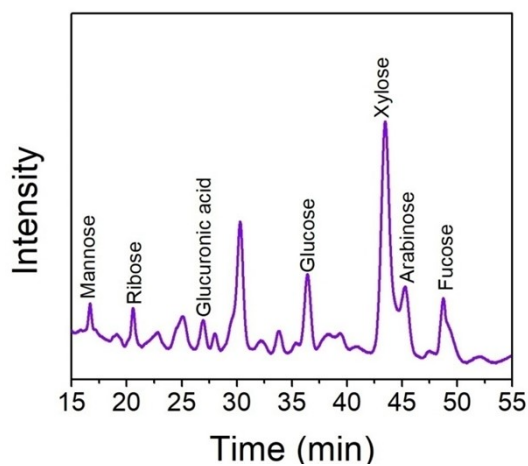

Figure S25. Liquid chromatography analysis for the sugar species as the decomposition products of α-cellulose after photocatalytic H$_2$ production reaction.
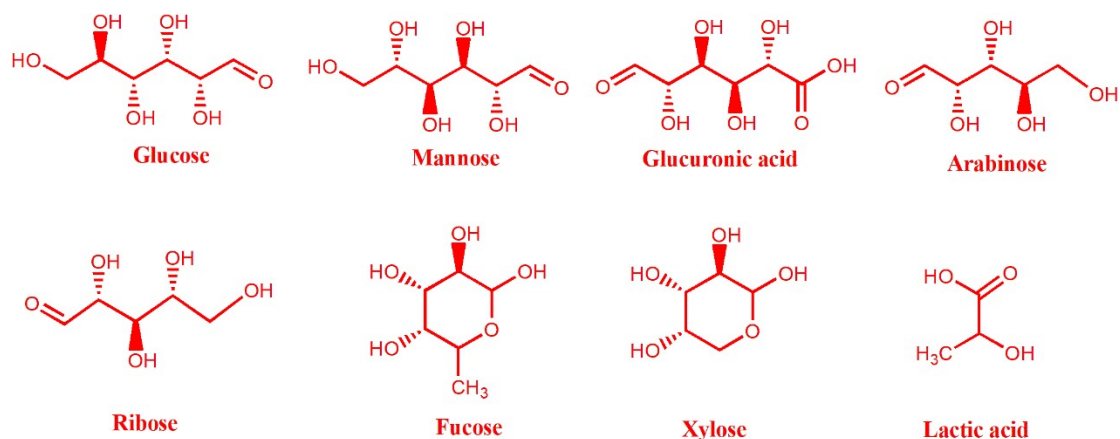
Figure S26. Chemical structure of decomposition products from α-cellulose after photocatalytic H₂ production reaction.

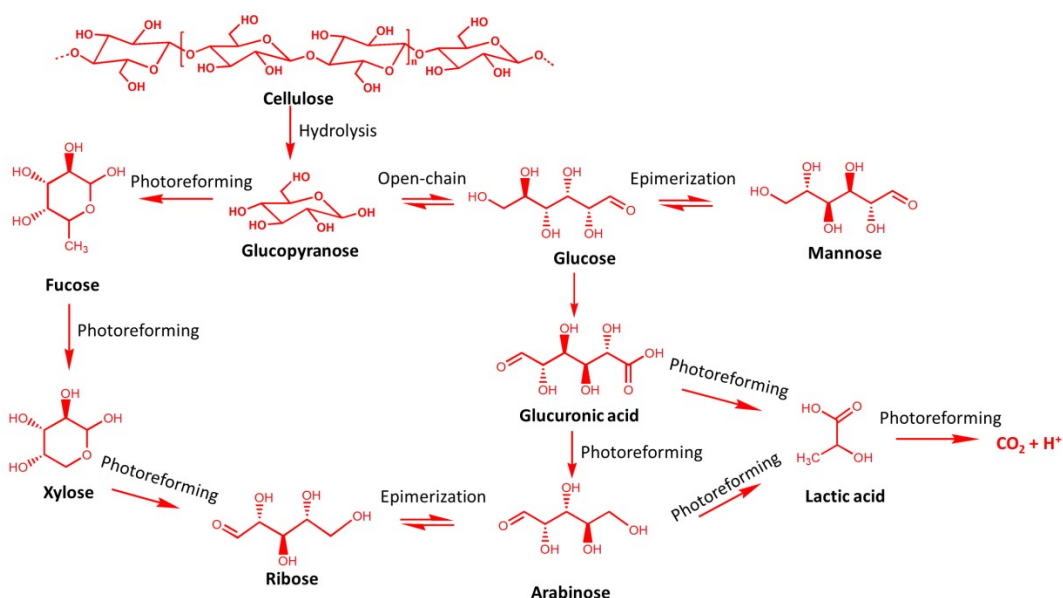**Figure S27**. Possible reaction mechanism for photocatalytic decomposition of α-cellulose. The cleavage of β-1,4-glycosidic bonds of α-cellulose could be realized by realized ˙OH radical during photocatalytic reaction, leading to formation of glucopyranose or glucose. And then the glucose could be converted small organic molecules even CO₂ by the ˙OH radical or photogenerated hole.
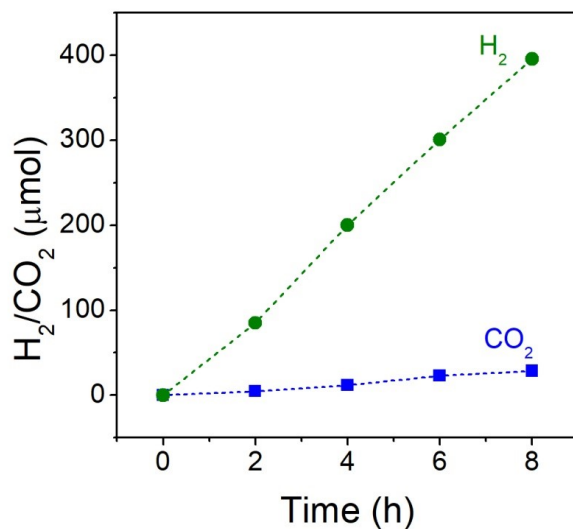
Figure S28. Comparison of photocatalytic H_2 and CO_2 generation over 0.4 Pt/TiO_2 photocatalyst. Photocatalytic reaction conditions: 100 mg photocatalyst, 300 W Xe lamp, 1g α-cellulose, 250 ml water.
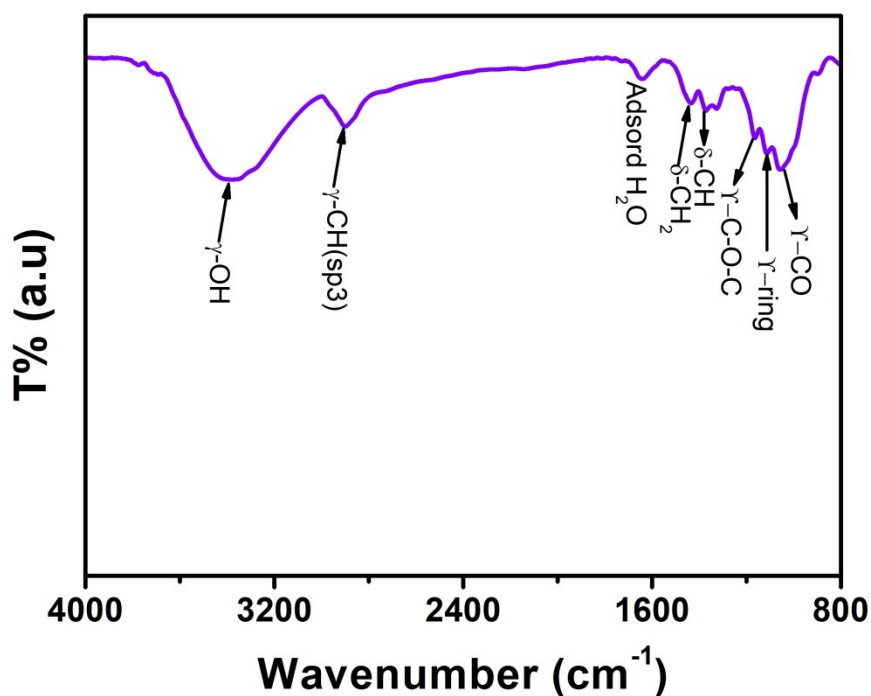

Figure S29. FT-IR spectra of residual α-cellulose after photocatalytic H_2 production reactio. It is obviously that residual α-cellulose exhibits surface groups of δ-C-OH, γ-CO, γ-ring, γ-C-O-C, δ-CH, δ-CH_2, γ-CH(sp$_3$), γ-OH, indicating that the surface of α-cellulose was constantly oxidizing during the photocatalytic reaction.
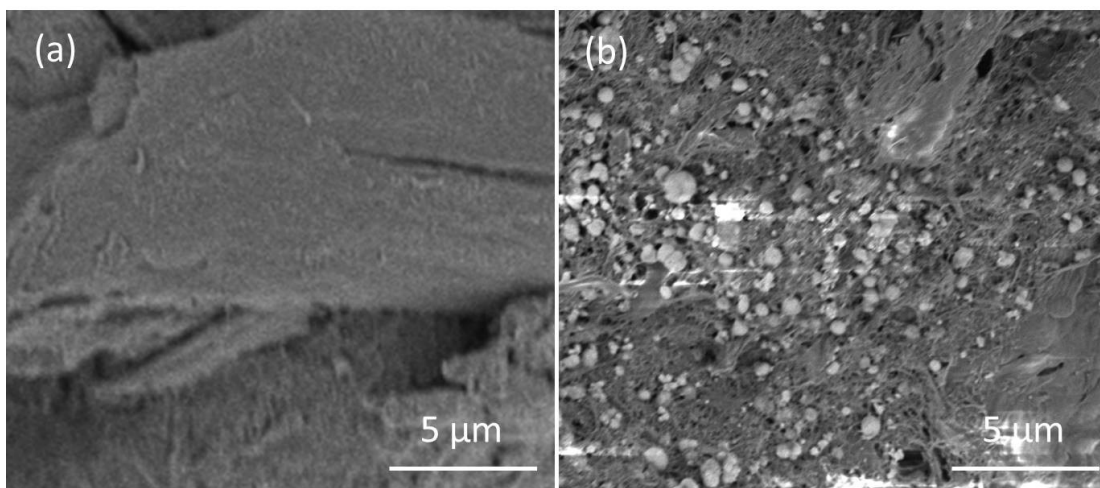
Figure S30. SEM images of fresh α-cellulose (a) and residualα-cellulose collected from photocatalytic H_2 production reaction (b).

Figure S31. Schematic diagram of photocatalytic H_2 production from lignocellulosic biomass over Pt/TiO_2 photocatalyst. Because the oxygen vacancy on the TiO_2 surface benefits the charge transfer across the Pt-TiO_2 interface as confirmed by DFT calculation, the photoexcited electrons in the CB of TiO_2 can rapidly transfer to Pt.

Table S1. Comparison of photocatalytic performance for H_2 production between the current work and other reported studies.
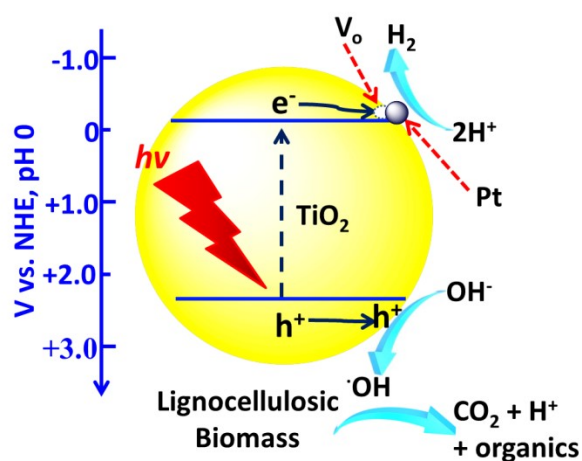
Enery	Photocatalyst	Sacrificial reagent.	Light source	H_2 evolution rate $(umol·h^{-1}·g^{-1})$	AQY(%)	ref
1	$RuO_2/Pt/TiO_2$	cellulose	Xe lamp	41		10
2	Pt/P25	cellulosic	AM 1.5	129	-	11
3	Pt/P25	rice husk suspension	AM 1.5	62.5	-	12
4	Pt/TiO_2	Cherry wood	Xe lamp	49	1.1	12
5	Pt/P25	celluloses	Xe lamp	~230	-	13
6	MoS_2/TiO_2	cellulose	Xe lamp	201	1.45(380 nm)	14
7	Pt/TiO_2	cellulose	UV-lamp	133		15
8	Pt/TIO_2 NSs	cellulose	Xe lamp	275	1.47 (380 nm)	16
9	$Pt/Cu-TiO_2$	cellulose	Hg lamp	510		17
10	$NiO_x//TiO_2$	cellulose	Hg lamp	270		18
8	Pt/TIO_2	cellulose	Xe lamp	494	3.21 (380 nm)	This work

References

1. G. Kresse, Furthmüller. *J. Phys. Rev. B* 1996, **54**, 11169.

2. G. J. Kresse, Furthmüller. *J. Comput. Phys. Sci*. 1996, **6**, 15-50.

3. J. P. Perdew, Burke, M. K. Ernzerhof. *Phys. Rev. Lett*. 1996, *77*, 3865-3868.

4. S. Grimme. *J. Comput. Chem*. 2006, **27**, 1787-1799.

5. P. E. Blöchl,. *Phys. Rev. B*, 1994, **50**, 17953.

6. G. Kresse, D. Joubert. *Phys. Rev. B*, 1999, **59**, 1758.

7. M. R. Hestenes, E. Stiefel. *J. Res. Natl. Bur. Stand*. 1952, **49**, 409.

8. H. J. Monkhorst, J. D. Pack. *Phys. Rev. B*. 1976, **13**, 5188.

9. V. Wang, N. Xu, J. C. Liu, G. Tang, W. T. Geng. Comput. *Phys. Commun*. 2012, **267**, 108033.   .

10. T. Kawai, T. Sakata. *Nature* 1980, **286**, 474-476.

11. A. Speltini. *Photoch. Photobio. Sci*. 2014, *13*, 1410-1419.

12. M. R. S. John, A. J. Furgala, A. F. Sammells. *J. Phys. Chem*. 1983, **87**, 801-805.

13. A. Caravaca, W. Jones, C. Hardacre, M. Bowker. *Proc. R. Soc. A*. 2016, **472**, 20160054.

14. P. Wang, Y. J. Yuan, Q. Y. Liu, Q. Cheng, Z. K. Shen, Z. T. Yu, Z. G. Zou,. *ChemSusChem* 2021, **14**, 2860-2865.

15. L. Lan, Y. Shao, Y. Jiao, R. Zhang, C. Hardacre, X. L. Fan. *Chin. J. Chem. Eng*., 2020, **28**, 2084-2091.

16. Q. Cheng, Y. J. Yuan, R. Tang, Q. Y. Liu, L. Bao, P. Wang, J. S. Zhong, Z. Y. Zhao, Z. T. Yu, Z. G. Zou. *ACS Catal*. 2022, **12**, 2118-2125.

17. S. Belda-Marco, M. A. Lillo-Ródenas, M. C. Román-Martínez, *Catal. Today* 2023, **413**, 113945.

18. L. Zhang, W. Wang, S. Zeng, Y. Su, H. Hao, *Green Chem.* 2018, **20**, 3008-3013.